PAPER

In situ diagnostics for nanomaterial synthesis in carbon arc plasma

To cite this article: B C Stratton *et al* 2018 *Plasma Sources Sci. Technol.* **27** 084001

View the article online for updates and enhancements.

Related content

- Complex structure of the carbon arc discharge for synthesis of nanotubes
  V Vekselman, M Feurer, T Huang et al.

- Recent advances in ultrafast-laser-based spectroscopy and imaging for reacting plasmas and flames
  Anil K Patnaik, Igor Adamovich, James R Gord et al.

- OH density measured by PLIF in a nanosecond atmospheric pressure diffuse discharge in humid air under steep high voltage pulses
  K Ouaras, L Magne, S Pasquiers et al.

Recent citations

- Pulsed anodic arc discharge for the synthesis of carbon nanomaterials
  Carles Corbella *et al*

IOP ebooks™

Bringing you innovative digital publishing with leading voices to create your essential collection of books in STEM research.

Start exploring the collection - download the first chapter of every title for free.

In situ diagnostics for nanomaterial synthesis in carbon arc plasma

B C Stratton[1] , A Gerakis[1,4], I Kaganovich[1], M Keidar[2], A Khrabry[1], J Mitrani[1,5], Y Raitses[1], M N Shneider[3] , V Vekselman[1] and S Yatom[1]

[1] Princeton Plasma Physics Laboratory, Princeton, NJ 08543, United States of America
[2] Dept. of Aerospace and Mechanical Engineering, The George Washington University, Washington DC 20052, United States of America
[3] Dept. of Mechanical and Aerospace Engineering, Princeton University, Princeton, NJ 08544, United States of America

E-mail: stratton@pppl.gov

Abstract

Developments in the recent application of *in situ* diagnostics to improve understanding of nanomaterial synthesis processes in carbon arc plasma are summarized. These diagnostics measure the plasma conditions in the arc core and the precursor species to nanoparticle formation and the presence and sizes of nanoparticles in the synthesis region surrounding the hot arc core. They provide information that could not be obtained by the *ex situ* diagnostics used in previous studies of nanomaterial synthesis in arc plasma. The following diagnostics are covered: optical emission spectroscopy, planar laser induced fluorescence, laser induced incandescence, fast frame imaging, coherent Rayleigh Brillouin scattering, and the nanomaterial extractor probe. The diagnostic measurements are consistent with a recently developed two-dimensional fluid model of nanomaterial synthesis in the arc plasma.

Keywords: nanomaterials, arc plasma, diagnostics

1. Introduction

Nanomaterials have unique mechanical, electrical, and optical properties that make them attractive for a wide variety of scientific and industrial applications. Thus, there is considerable interest in developing nanomaterial synthesis techniques with high yield, selectivity, and material quality. Carbon-based nanomaterials include fullerenes, single- and double-walled carbon nanotubes, graphene, and nano-fibers. These nanomaterials and others, including non-carbon-based materials, can be synthesized by chemical vapor deposition (CVD), laser ablation [1, 2], and in arc plasma [3, 4]. CVD is currently the most widely used commercial process for nanomaterial synthesis. In CVD synthesis, nanomaterials are grown on the surface of a substrate. In laser ablation and arc plasma synthesis, the nanomaterials can grow in the gas phase

(volume growth), which has the desirable feature of producing nanomaterials in powder form. Arc plasma synthesis is attractive for this reason and for its simplicity and relatively low cost: arc plasma is created between two electrodes and material ablated from the electrodes evaporates to become the feedstock for nanomaterial synthesis in the gas phase. The expensive lasers and associated equipment required for laser ablation synthesis are not needed for arc plasma synthesis. However, the selectivity of arc plasma synthesis is generally poor compared to the selectivity of CVD synthesis. Improvement of nanomaterial selectivity in arc plasma synthesis requires better understanding of the synthesis process, which is presently not well understood.

Previous studies of arc plasma synthesis of nanomaterials have relied on analysis of the produced nanomaterials as the primary diagnostic technique: the synthesized nanomaterials are collected from the cathode and walls of the arc chamber and are characterized by a variety of *ex situ* analysis techniques such as electron microscopy (SEM and TEM), Raman spectroscopy, x-ray spectroscopy. However, this approach provides incomplete information because in-volume

---

[4] Currently at Department of Aerospace Engineering, Texas A&M University, College Station, TX 77843, USA.
[5] Currently at Lawrence Livermore National Laboratory, Livermore, CA 94550, USA.

**Table 1.** *In situ* diagnostics for arc plasma synthesis of nanomaterials.

Diagnostic	Quantities measured	References
Optical emission spectroscopy (OES)	Species identification, spectral line intensities, plasma electron temperature and density	[11]
Fast frame imaging (FFI)	Fast 2D images of spectral line intensities, time-resolved discharge dynamics	[11–13]
Planar laser induced fluorescence (PLIF)	Species concentrations (2D)	[11, 14]
Laser induced incandescence (LII)	Nanoparticle sizes, images of nanoparticle distributions	[15, 16]
Coherent Rayleigh Brillouin scattering (CRBS)	Nanoparticle masses, distribution functions, and concentrations	[17, 18]
Nanomaterial extractor probe	Nanoparticles extracted from synthesis region for *ex situ* analysis	[19]

nanomaterial synthesis is not directly observed. In particular, *ex situ* analysis of the synthesized nanomaterials does not provide information on the plasma conditions and the precursor species to nanoparticle formation. (See [3–8] for examples of previous studies.) Probes and optical emission spectroscopy (OES) were used to provide *in situ* measurements in some earlier experiments [9, 10]. Thus, improved understanding of nanomaterial synthesis requires more extensive *in situ* measurements in the synthesis region. In the Laboratory for Plasma Nanosynthesis (LPN) at the Princeton Plasma Physics Laboratory, we have focused on developing diagnostics to provide these *in situ* measurements and utilizing them with modeling to gain understanding of the synthesis processes.

This paper summarizes our work on developing and using these *in situ* diagnostic techniques to gain understanding of nanomaterial synthesis processes. Following a brief description of the experimental arrangement for carbon arc plasma synthesis of nanomaterials, the following *in situ* diagnostic techniques are described: OES, planar laser induced fluorescence (PLIF), laser induced incandescence (LII), fast frame imaging (FFI), coherent Rayleigh Brillouin scattering (CRBS), and the nanomaterial extractor probe. The properties measured by these diagnostics are listed in table 1 along with references to our publications on them. These diagnostics provide spatially-resolved measurements. This is important because there is a strong gradient in the plasma and gas temperatures, with lower temperatures at larger distances from the arc axis [11]. As a result, the dominant species present change with spatial location. Although most of these diagnostics have been previously used in other contexts, the combined set of measurements is important to advancing understanding of nanomaterial synthesis.
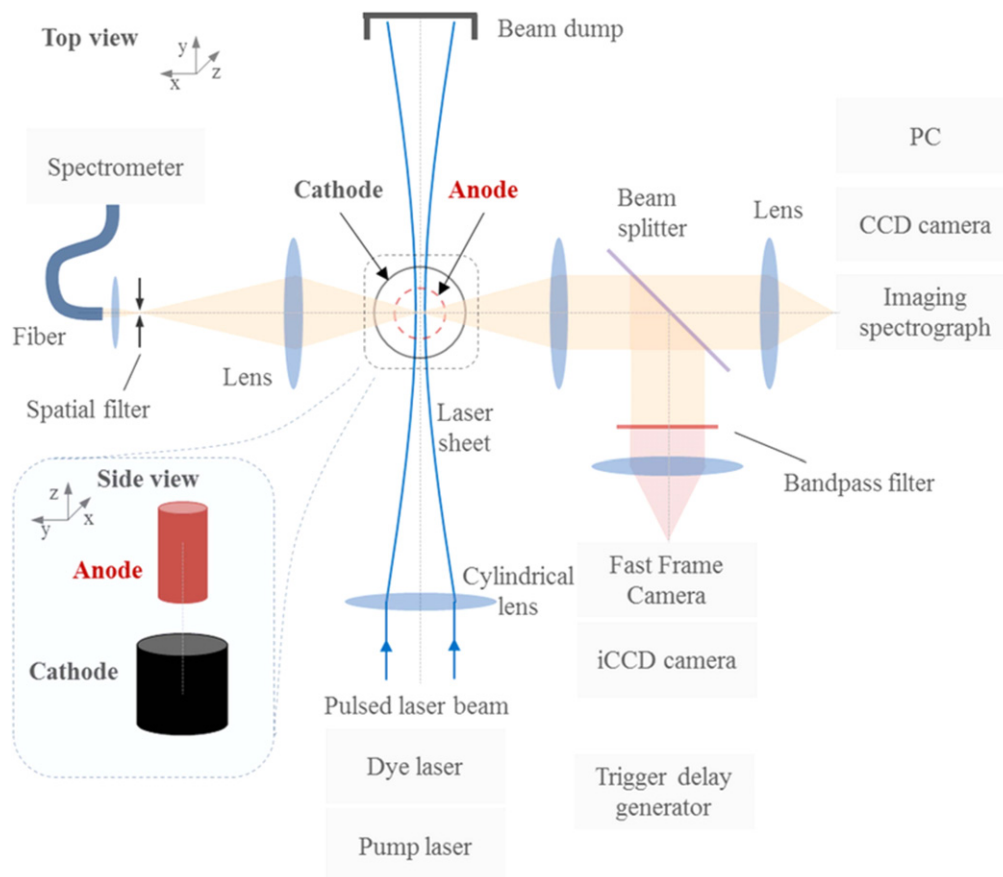
2. Arc plasma experimental arrangement

The carbon arc setup consists of two cylindrical graphite electrodes that are oriented vertically or horizontally in an arc reactor chamber filled with helium gas at a pressure of ∼500 Torr [20–22]. The arc setup is shown schematically in figure 1. In most of the experiments, the diameter of the cathode is larger than that of the anode, with typical values of 5.0–6.5 mm for the anode and 9.5–11.5 mm for the cathode.
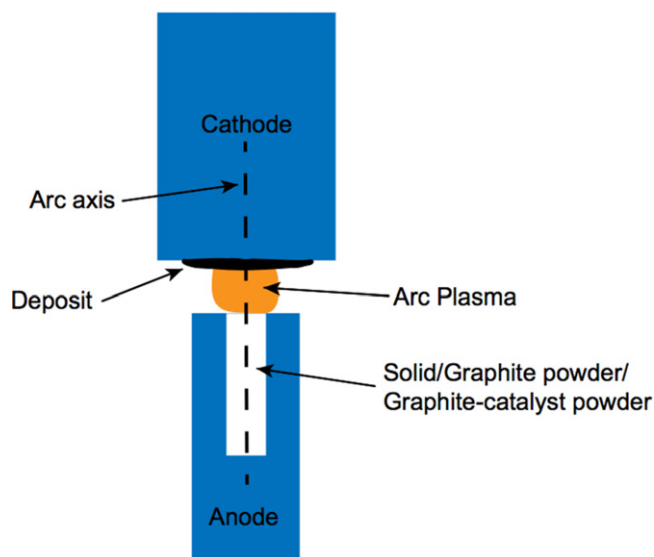
Figure 1. Schematic of carbon arc plasma setup for nanomaterial synthesis.

The cathode is solid graphite, while the anode can either be solid graphite or have a coaxial hole that is packed with pure graphite powder or a mixture of graphite and catalyst metal powders (e.g., nickel and yttrium). The latter configuration is used to synthesize single walled carbon nanotubes (SWCNTs) while the pure graphite anode configuration produces other types of nanomaterials [5–7]. In the case of a solid graphite anode, the synthesized nanomaterials are deposited primarily on the cathode.

The arc is initiated by bringing the electrodes into contact and then gradually separating them via a stepping motor-driven mechanism, which is also used to maintain a fixed anode–cathode gap in the 2–4 mm range. Power is provided by a current-regulated power supply with a ballast resistor in series with the electrodes to reduce relaxation oscillations due to the negative differential resistance of the arc. Depending on the experiment, the arc current is in the 40–60 A range and the voltage drop is in the 20–30 V range. The duration of an arc experiment is typically about 2 min and is determined by heating of the reactor chamber. The plasma column is confined to the region between the anode and cathode and has a diameter of ∼6 mm. The gas temperature in the plasma core is 8000 K [11, 23]. The gas temperature drops rapidly outside

Figure 2. Schematic of arc plasma experimental setup with optical emission spectroscopy, fast frame imaging, and planar laser induced fluorescence diagnostics (from [11]).

the plasma with values of 4500 K at 3 mm and 3500 K at 4 mm. Our work shows that nanomaterial growth occurs primarily in the region outside the plasma core [23]. The *in situ* diagnostics described in this paper probe both the plasma core and the hot gas region.

3. Optical emission spectroscopy

OES was used to measure the plasma electron density and temperature in an arc that utilized horizontal solid graphite anodes and cathodes, with diameters of 6.5 mm and 9.5 mm, respectively [11].

The arc was operated in a helium atmosphere at 500 Torr pressure with 5% hydrogen by weight added to enable the OES measurements. Experiments were performed in both the low- and high-ablation modes of arc operation, which are distinguished by the arc current and ablation rate of the anode [20].

The experimental arrangement for these measurements, and the FFI and PLIF measurements described below is shown in figure 2 and the experimental details are given by Vekselman *et al* [11]. The optical axes of the low—(0.22 nm pixel^{-1}) and the imaging high-resolution (0.0046 nm pixel^{-1}) spectrometers used for OES and PLIF detection, the PLIF laser, and the FFI system intersected the

arc axis at right angles at a point midway between the electrode surfaces. The plasma was imaged onto the entrance slit of the high-resolution spectrometer with the radial direction in the arc discharge along the long dimension of the slit. The light collection optics had a magnification of $M = 1/4$, yielding a spatial resolution of 120 pixels mm^{-1} on the CCD camera detector (4.8 μm $\times$ 4.8 μm pixels). The time resolution of the measurements was 6–20 μs, determined by the camera exposure time.

The low-resolution spectrometer measured spectra in the visible region (380–700 nm), with the dominant features being the C_2 Swan bands and the H_α, H_β, and H_γ lines (shown in figure 3 of [11]). Weaker lines of carbon atoms and ions were also observed. The dominance of the C_2 Swan bands is typical in spectra of carbon arcs and is consistent with carbon dimers and trimmers being important precursor species in the nanomaterial synthesis process.

Spatially-resolved measurements of the electron density profile in the low- and high-ablation modes were derived from measurements of the H_α line shape obtained using the high-resolution spectrometer [24, 25]. A spectrum measured with the arc operated in low-ablation mode (arc current = 55 A) is shown in figure 3 [11] along with a fit to a Voigt function. The Voigt function is the convolution of a Gaussian line profile due to instrumental broadening and Doppler broadening caused by ion motion and a Lorentzian line profile due
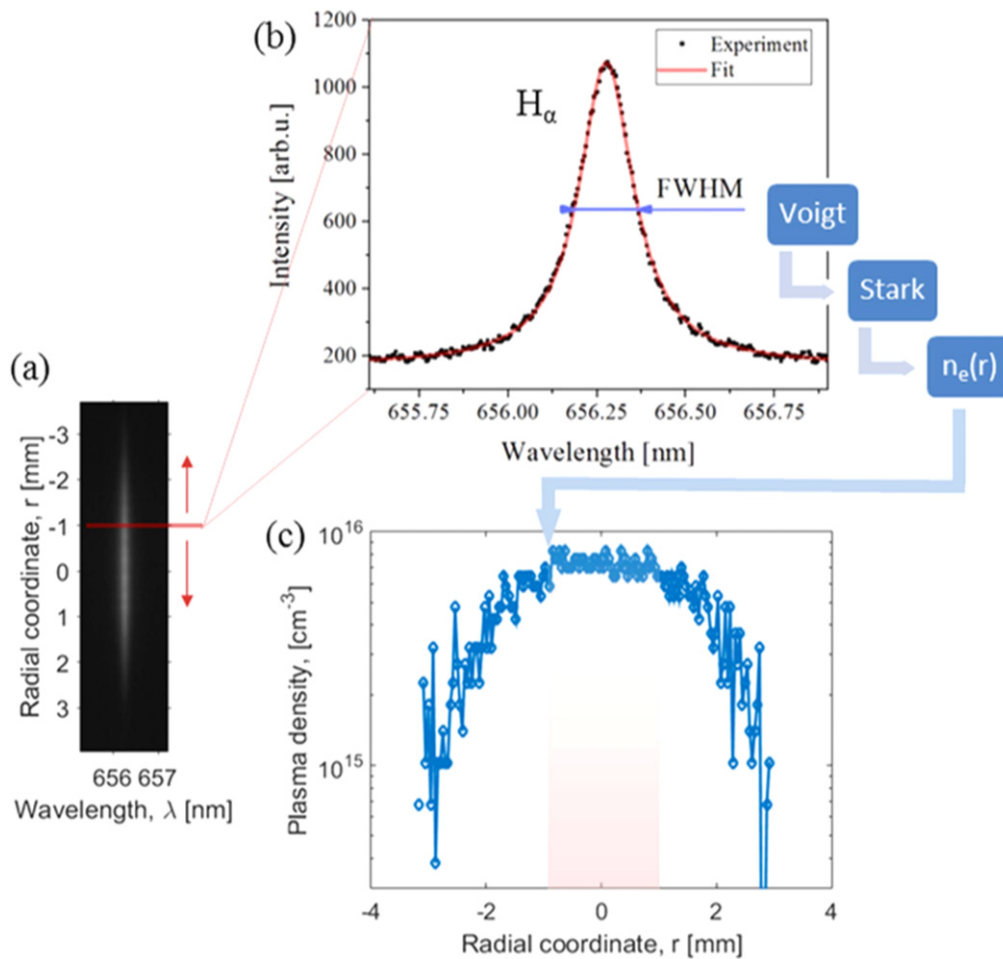
Figure 3. Electron density profile measurement in low-ablation mode of arc operation showing: radial profile of H_α emission (a); measured line profile at $r = 1$ mm fit to a Voigt function convolved with the instrumental profile (b); and the derived electron density profile (c). (From [11].)

to Stark broadening. The contribution due to Doppler broadening was estimated from the temperature measured using the Boltzmann diagram method described below. To ensure that the line profile measurement was not distorted by self-absorption effects, the H_α line was verified to be optically thin by doubling the emission using a spherical mirror placed behind the arc plasma in the spectrometer line of sight. The electron density profile shown in figure 3 is flat with a value of 8×10^{15} cm^{-3} inside a central region of radius $\sim$1 mm and drops rapidly at larger radii. Similar measurements performed in high-ablation mode (arc current = 65 A) show a larger electron density of 2×10^{16} cm^{-3} inside the central region.

The electron temperature was measured by fitting the relative intensities of the H_α, H_β, and H_γ lines measured by the low-resolution spectrometer to a collisional-radiative model [11, 24, 25]. This approach is a generalization of the Boltzmann diagram method that does not assume that the upper levels of these lines are in local thermodynamic equilibrium, which is not a valid assumption for the arc plasma. Electron temperature values of 0.8 ± 0.1 eV were obtained for the low-ablation mode and 0.9 ± 0.2 eV for the high-ablation mode. In both cases, the values were constant in time

following a transient at arc initiation. The time resolution of these measurements was determined by the 1 μs exposure time and the spatial resolution was determined by the observational cone cross-sectional area in the focal plane of $\sim$0.8 mm^2 [11].

These values of the electron density and temperature are applicable to the experiments described below. (It was not possible to measure the electron temperature and density in each individual experiment due to the time required.)

4. Fast frame imaging

The FFI diagnostic consists of a high-speed visible camera that views the arc plasma through a macro lens and broadband interference filters that are centered on lines of C_2 (470 nm), C I (600 nm), and H (656.3 nm). The time resolution of the measurements was 2 μs, determined by the camera exposure time. The light collection optics determined the spatial resolution of 24 pixels mm^{-1} on the camera (22 μm $\times$ 22 μm pixels).

This system produced the 2D images of the brightness at these wavelengths shown in figure 4 [11]. It is clear that the
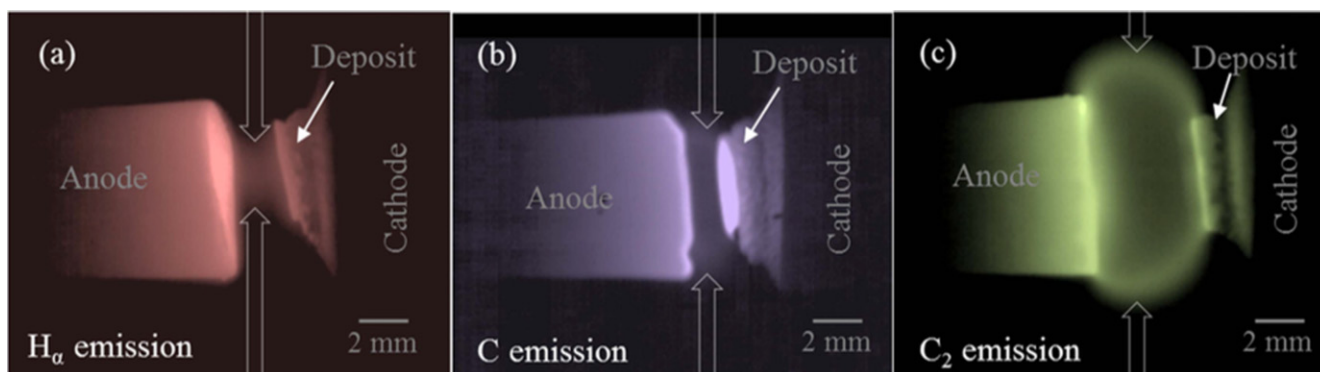
Figure 4. FFI images of H_α (a), C I (b), and C_2 (c) line brightnesses with the arc operated in the low-ablation mode (from [11]).
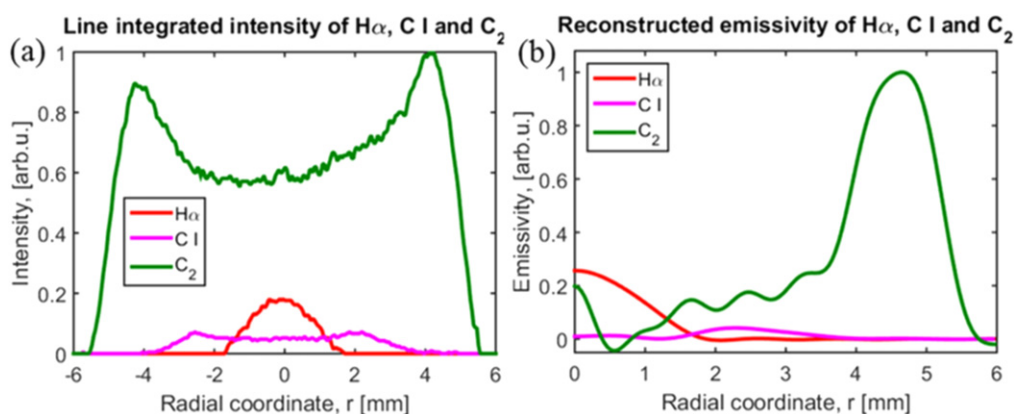
Figure 5. (a) Radial profiles of the H_α, C I, and C_2 line brightnesses taken from figure 4 in the center of the electrode gap; (b) reconstruction of the line emissivities assuming rotational symmetry (from [11]).

H_α emission is concentrated in the arc core, while the C I line is emitted from a broader region, and the C_2 emission is from an even larger region that extends significantly outside the anode. This is due in part to the larger excitation energies for the H_α (12 eV) and C I lines (10.7 eV) compared to the excitation energy for the C_2 band (2.6 eV), but it is also due to differences in the spatial distributions of these species. As shown in figure 5, Abel inversion of the these line brightnesses assuming rotational symmetry confirmed that the C_2 emission originates predominantly from a much larger radius than the H_α and C I emission.

The FFI technique also provides valuable information on the arc motion, which can be significant, especially in the high-ablation mode. An example of this is the observation by Yatom *et al* [12] of the 'synthesis-on' and 'synthesis-off' modes in the synthesis of SWCNTs using a hollow anode filled with C–Ni–Y powder (14:4.1:1 by weight). FFI images of the arc motion taken through the C_2 filter showed that, for the majority of the arc operation period, the plasma was attached to the solid edge of the anode and therefore was not in contact with the catalyst required to synthesize SWCNTs. Movable witness plate measurements showed little synthesis of SWCNTs during this 'synthesis-off' mode of operation. The arc occasionally attached to the center of the anode and the powder material entered the plasma ('synthesis-on' mode), producing a much larger quantity of SWCNTs as found in witness plate samples taken during this time.

Witness plates are removable plates that can be located in the synthesis region to collect particle samples for later *ex situ* analysis. OES measurements showed more intense C_2 Swan band emission and the presence of catalyst Ni and Y atomic lines in 'synthesis-on' mode compared to 'synthesis-off' mode. FFI was also used to study the unstable behavior of the arc discharge by Gershman and Raitses [13].

5. Planar laser induced fluorescence

The OES measurements discussed above show that C_2 exists primarily in a peripheral region surrounding the arc plasma (referred to as the 'bubble'). This supports the hypothesis that carbon is ablated from the graphite anode in the form of molecules and larger particles which are then dissociated to carbon atoms in the hot arc core and then associate back to C_2 and C_3 in the hot gas region (3000–5000 K) surrounding the arc plasma. To further develop a model of nanomaterial synthesis, it is necessary to perform quantitative measurements of the C_2 density for comparison with model predictions. PLIF is well-suited to this measurement because it is a sensitive species-specific technique with high spatial and time resolution that can be calibrated to be quantitative. The principles of laser induced fluorescence as applied to C_2 detection in low temperature plasmas are described in [26–28]. Because signal detection is at a different wavelength
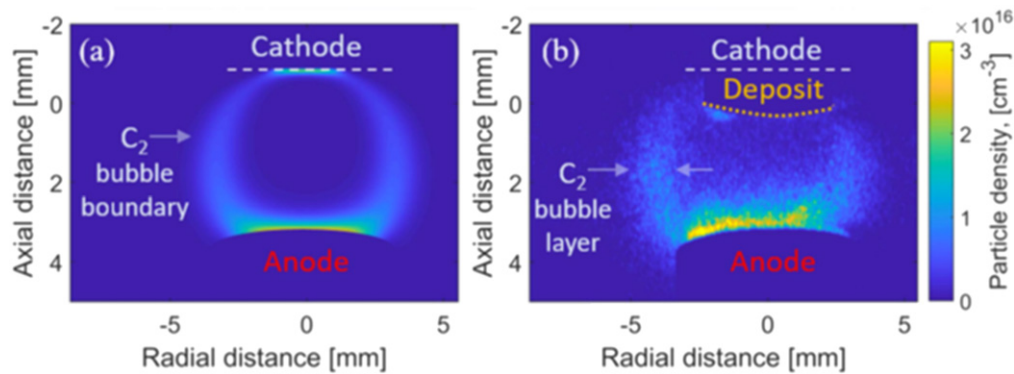
Figure 6. Simulated (a) and measured C$_2$ density distribution in carbon arc (from [14]).

from the laser wavelength, PLIF is insensitive to scattered laser light, which can be significant in the arc environment. The small background light contribution to the signal is due only to plasma emission. PLIF differs from conventional single-point LIF in that 2D images of the fluorescence are measured.

Vekselman *et al* [11, 14] performed quantitative PLIF measurements of the 2D C$_2$ distribution in a carbon arc experiment using a setup similar to that shown in figure 2. The beam from a dye laser pumped by a frequency-tripled Nd:YAG laser with 8 ns pulse duration was formed into a sheet beam (6 mm high by 0.05 mm wide) by a cylindrical lens that was aligned with the arc axis. The dye laser operated with a linewidth of 0.06 cm^{-1} and was tuned to excite the (3, 1) Swan band at 437.14 nm. The dye laser energy of 10 mJ per pulse was attenuated to $\sim$0.1 mJ by a half-wave plate and rotatable linear polarizer to avoid saturation of the upper level of the transition. A 2D image of the fluorescence near 469 nm was measured using an intensified CDD camera coupled to an objective lens and interference filter. The spatial resolution was 36 pixels mm^{-1}. The camera exposure time of 40 ns determined the time resolution of the measurements and was chosen to match the duration of the fluorescence signal to minimize the contribution of background light to the signal. The background signal measured with the laser off was subtracted from the fluorescence signal. Calibration of the system sensitivity and measurement of the excited state lifetime were required to derive quantitative measurements of the C$_2$ density from the images. This procedure is described in detail in [14].

A PLIF measurement of the C$_2$ density distribution compared with a 2D fluid model prediction for an arc with solid graphite electrodes operated at 50 A is shown in figure 6 [14]. Both the measurement and the model show the bubble-shape inferred from the OES measurements and the absolute values are in good agreement. The model accurately reproduces the C$_2$ bubble size and thickness and the formation of C$_2$ near the anode surface seen in the measurements. The details of the model are given in [14, 23]. It is based on a fluid model of the plasma coupled to a diffusive transport model for carbon species. The model does not account for the change in the cathode surface topology due to the growth of the deposit seen in figure 6(b).

6. Laser induced incandescence

In addition to measurements of the plasma composition, direct observation of the nanoparticles in the arc plasma and surrounding hot gas region is required to identify the region where nanoparticle synthesis occurs. For larger nanoparticles and microparticles with diameters greater or equal to than $\sim$5 nm, this is accomplished using LII. A short duration laser pulse heats the nanoparticles to a high temperature and the time evolution of the emitted incandescence radiation is detected [15, 16, 29]. The decay rate of the incandescence is dependent on particle size and temperature, with smaller particles exhibiting faster decay rates. LII can therefore serve as a particle size diagnostic when coupled to a suitable model of the incandescence. LII has been primarily applied to particle measurements in combustion; a review is given in [29].

Yatom *et al* [16] measured particle sizes as a function of radius from the arc axis in an arc with solid graphite electrodes that was operated at 60 A. A Nd:YAG laser (1064 nm wavelength) with 8 ns pulse duration was injected into the arc region. The laser beam was shaped and clipped to yield a near-circular, flat-top profile with a radius of 5 mm and energy of 25 mJ/pulse. The time evolution of the incandescence was observed with a photomultiplier tube (PMT) and a broadband interference filter centered at 690 nm. The light imaged onto the PMT passed through a slit with variable width and position relative to the arc axis. This allowed the radial profile of the LII signal to be measured. (The experimental setup is shown in figure 1 of [16].) LII signals were measured for distances from the arc axis from $r = 1$ mm to $r = 13$ mm with a slit width corresponding to 2.25 mm in the radial direction. This slit width defines the spatial resolution of the measurement in the radial direction. A tall slit was used so there no spatial resolution in the vertical direction. The laser repetition rate was 2 Hz, which allowed $\sim$200 LII signals to be collected and averaged during the 2 min duration of an arc run. The LII signals with good signal to noise ratios were selected and a low pass filter was applied to remove the high frequency noise due to the background arc light. The signals were then normalized to the same peak value and averaged to yield a characteristic LII time evolution for each radial location. The time resolution of the measurement is
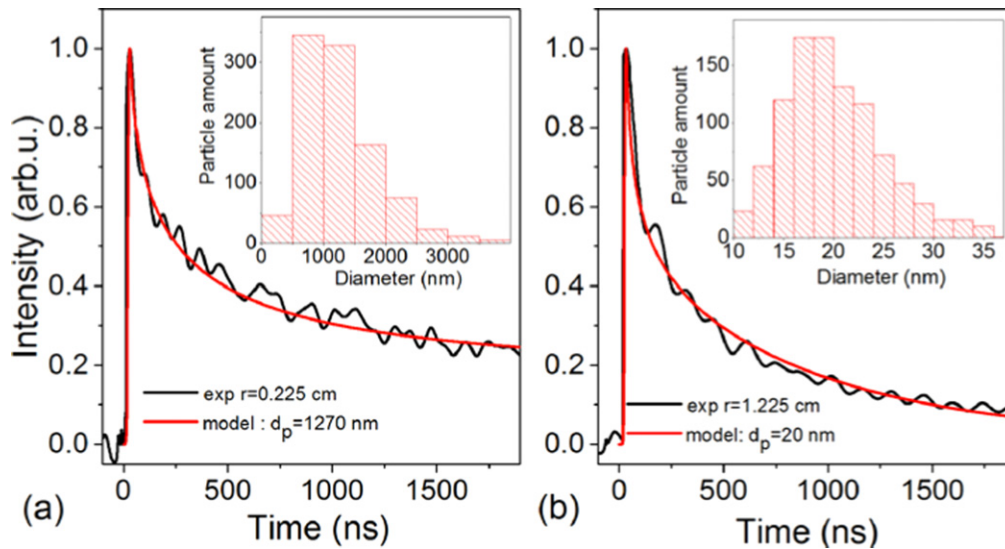
**Figure 7.** Measured and fitted LII signals at $r = 2.25$ mm (a) and $r = 12.25$ mm (b) (from [16]).

several microseconds and is determined by the time required for the incandescence to completely decay away.

The detection limit of the LII measurement is evaluated via the approach described in [30]. The calculation considers the total power radiated by spherical particles and is converted to the voltage on a $50\,\Omega$ load, taking into account the geometry, the sensors employed in our experimental setup, and the form of the laser beam. A detectable signal level of several mV corresponds to a particle number density of $10^8\,\mathrm{cm}^{-3}$.

Measurements of the LII signals at $r = 2.25$ mm and 12.25 mm are shown in figure 7 [16]. The signal at $r = 12.25$ mm has a faster decay rate than the signal at $r = 2.25$ mm, indicating that particle size decreases with radial location. The average particle size was derived from the LII signals using a model that solves the time-dependent energy and mass balance equations for the particles. The details of the model are given in [16] and the references therein. The dominant processes for energy balance are heat transfer due to laser absorption, conduction, oxidation, radiation, sublimation, thermionic emission, and radiation from the arc plasma. Mie theory is used to calculate the particle heating rates due to laser absorption, radiation, and arc plasma radiation.

The model simulates the LII signal from an assumed distribution of spherical particle diameters and this distribution then is modified to achieve good agreement with the measured LII signals. Two other important inputs to the model are the gas temperature and the initial particle temperature before laser heating. These are simulated using the model described in section 5 above. The results of this model fitting are shown in figure 7. The best fit was found with mean particle diameters of $1.27\,\mu$m at $r = 2.25$ mm and 20 nm at $r = 12.25$ mm. A log-normal distribution of particle diameters (shown in the insets in figure 7) with a standard deviation of 50% was assumed.

The mean particle diameter as a function of radius from the arc axis measured in this way is shown in figure 8 [16].
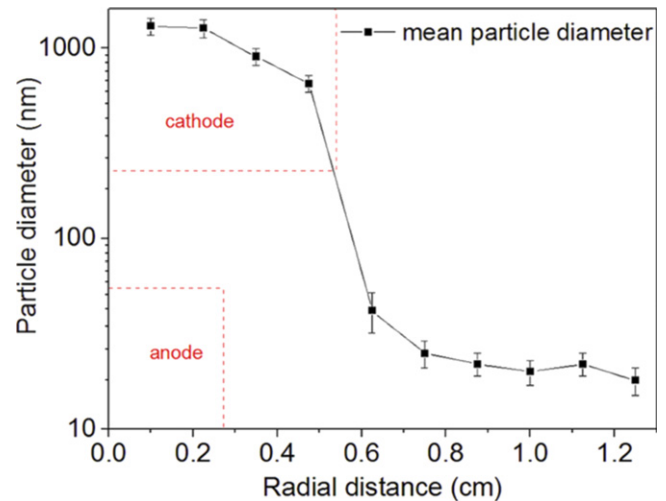
Figure 8. Mean particle diameter obtained by fitting LII measurements as a function of radial distance from the arc axis (from [16]).

The mean particle diameter is on the order of $1\,\mu$m for radii inside the cathode radius; it drops sharply to much smaller values of 20–30 nm outside the cathode radius. A heat transfer simulation shows that this behavior can be explained by a model in which large ($\sim$1 μm) carbon particles are ablated from the anode due to thermal stresses caused by the arc attachment point and completely evaporate within 1 mm of radial motion. These large particles are therefore found only inside the cathode radius. The smaller particles found outside the cathode radius are formed by clustering of carbon atoms and molecules (e.g., C_2 and C_3), not by evaporation of larger particles. It is important to note that the LII model provides a measurement of the mean particle diameter assuming spherical particles. In reality, the particles are not all spherical, e.g., carbon nanotubes are cylindrical, and would require a different model. However, the approximate sizes and trends provide useful information regardless of particle shape.

7. Coherent Rayleigh Brillouin scattering

The LII technique is capable of detecting particles with diameters down to approximately 5 nm, but it is not applicable to smaller particles. This leaves a gap in measurement capability between particles of this size and the small molecules and atoms observed by OES and PLIF. CRBS is a four-wave mixing laser scattering technique that has been previously applied to gases [17, 31–34] and has recently been applied to small nanoparticles [18]. In CRBS, two pump laser beams intersect at an angle close to 180°, creating an interference pattern. Upon interaction with a medium, an optical lattice is created since small particles are trapped on the high intensity nodes of the interference pattern due to electrostriction. A probe laser beam that is shone on this induced lattice at an angle fulfilling the Bragg condition is scattered from the trapped particles, producing a signal beam that maintains all the characteristics of the probe beam, i.e. it is a laser beam. (The scattering geometry is shown in figure 2 of [18].) In general, the signal line profile consists of a peak due to Rayleigh scattering and two peaks due to Brillouin scattering. An important feature of CRBS is that the signal is a coherent collimated beam and is therefore much stronger than the isotropic emission produced by spontaneous Raleigh scattering.

Theoretical analysis shows that CRBS should be able to detect small concentrations of nanoparticles in a buffer gas [35]. The relative contribution to the CRBS signal from nanoparticles with density N_n compared to the CRBS signal from the buffer gas with density N_g are comparable when $N_n/N_g \propto (\alpha_g/\alpha_n)^{5/2}$, where α_n and α_g are the polarizabilities of the nanoparticles and the buffer gas atoms, respectively. (This dependence of the intensity of the CRBS signal for gases with different polarizabilities was experimentally confirmed in [17].) For example, for a mixture of C_{60} molecules and Ar atoms at atmospheric pressure and 300 K, C_{60} can be detected at a partial pressure of 1 mTorr ($N_n \sim 3.3 \times 10^{13}$ cm^{-3}). If the buffer gas is helium, the minimum detectable C_{60} partial pressure is of the order of 5×10^{-6} Torr ($N_n \sim 1.6 \times 10^{11}$ cm^{-3}). For larger nanoparticles, the minimum detection limit is much lower.

The CRBS experimental setup is described in detail in [17, 18]. It consists of two Nd:YV04 pump laser beams (1064 nm wavelength) with pulse duration of 150 ns and energy of 250 mJ/pulse. The system utilizes the single-shot chirped lattice approach to vary the velocity of the optical lattice during a single laser pulse. The CRBS beams cross at a point located at $r = 13$ mm from the arc axis. A non-planar scattering geometry is used to minimize the contribution to the signal beam of scattered background light from pump beams. The spatial resolution of the measurement is determined by the spatial extent of the CRBS interaction region, which is approximately 0.15 mm [18].

The measured CRBS spectrum plotted versus optical lattice velocity was constructed from laser pulses with different chirp rates and is shown in figure 9 [18]. Each point in figure 9 is the CRBS signal from a single laser shot with background removed. The Brillouin peaks are negligible
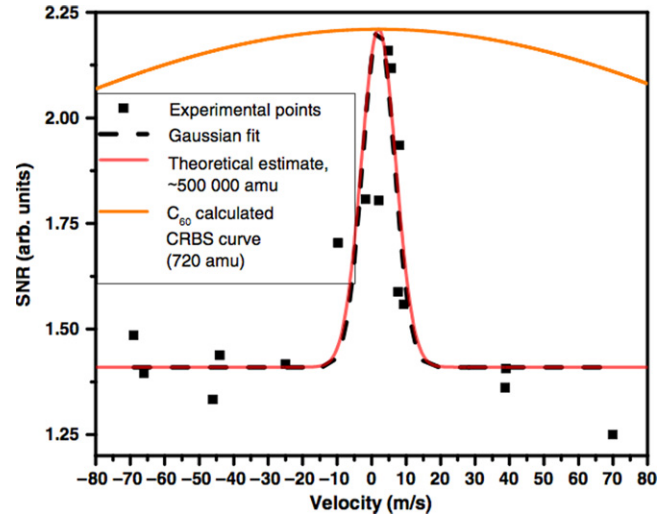
Figure 9. Measured CRBS nanoparticle Rayleigh profile measured at $r = 13$ mm relative to arc axis. It is well reproduced by a theoretical estimate (red curve) that assumes a particle mass of 5×10^5 amu and that the nanoparticles are in thermal equilibrium with the ambient gas at 1500 K. A calculated Rayleigh profile for C_{60} particles (720 amu mass) is shown for comparison (orange curve). (From [18].)

because phonons cannot be launched at low nanoparticle densities. The measured spectrum is fit to a Doppler line profile. The mass of the nanoparticles was estimated to be 5×10^5 amu assuming that the particles are in thermal equilibrium with the ambient gas at a temperature of 1500 K at $r = 13$ mm predicted by the 2D simulations discussed above. This corresponds to a spherical particle diameter of 6 nm assuming the graphite particles are hollow or 5 mm assuming that they are solid graphite. Thus, the CRBS measurements show the existence of very small nanoparticles in the region outside the arc core where nanoparticles synthesis is believed to occur. We note that the measured line profile is dominated by the lighter particles that are present in significant quantities since they exhibit the largest Doppler broadening.

With the present setup, the laser energies required to obtain measurable CRBS signals resulted in the destruction of the nanoparticles early in the laser pulse; thus, the measured nanoparticle sizes are characteristic of the particle sizes prior to the laser pulse. Improvements to the sensitivity of the system that should eliminate this problem have been identified, e.g., using a probe beam at a different wavelength than the pump beams and spectral filtering should significantly reduce the background light and allow measurements to be made at lower laser energies. A potential future application of CRBS is to measure the flow velocity, an important parameter for understanding the synthesis process because it determines the nanoparticle residence time in the synthesis region. We note also that Santra *et al* [36] have shown theoretically that it should be possible to measure nanoparticle concentrations and shapes (based on depolarization) using spontaneous Rayleigh Brillouin scattering.
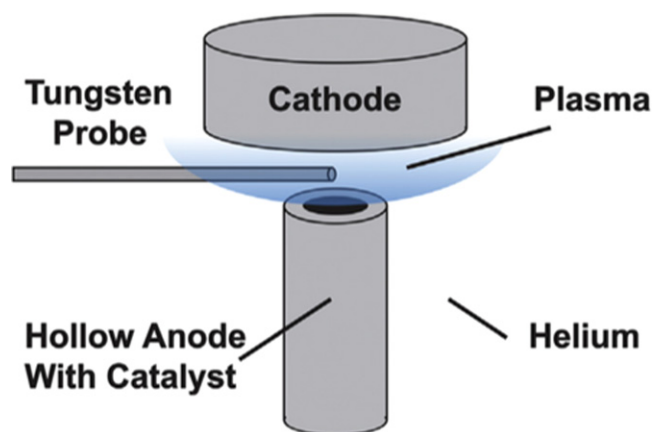
Figure 10. Schematic of the nanomaterial extractor probe concept. (From [19].)

8. Nanomaterial extractor probe

The LII and CRBS techniques provide *in situ* measurements of nanoparticle sizes and help identify the region of nanomaterial formation but they do not provide detailed information on the structure of the nanoparticles at various locations. Such structural information is obtained using a nanomaterial extractor probe that collects nanomaterial samples from the nanomaterial formation region [19]. The collected samples are then analyzed *ex situ* using standard techniques such as Raman spectroscopy and electron microscopy. The nanomaterial extractor probe is shown schematically in figure 10. It consists of a thin tungsten wire that can be rapidly moved through region surrounding the hot plasma core by a high-speed actuator. A signal generator drives the probe and can be programed to allow the probe to be exposed to the plasma for a specified residence time. A shield protects the probe from plasma exposure at other times.

Such a system was used to study SWCNT formation in an arc with a graphite cathode (13 mm diameter) and a hollow graphite anode (5 mm diameter) containing graphite–nickel–yttrium powder (94.8:4.2:1 molar ratio) [19]. The arc was operated at 75 A current with a gap of 2 mm. The probe was a tungsten wire (0.5 mm diameter and 50 mm length). Nanomaterial samples were collected over the region $r \geqslant 3$ mm from the arc axis to avoid melting of the probe and residence times of 10–60 ms were used. The collected nanomaterial samples were analyzed by Raman Microscopy and SEM. This experiment determined that SWCNT growth occurs primarily in the $r = 3$–11 mm region and that the SWCNT length increases monotonically up to 500 nm with increasing distance from the arc axis, while diameter and chirality varied only slightly with position [19].

9. Summary and conclusions

The *in situ* diagnostic techniques described here have led to advances in understanding of nanomaterial synthesis processes in carbon arc plasmas that were not possible in previous studies that utilized mainly *ex situ* diagnostics. In

particular, these measurements are consistent with a recently developed two-dimensional fluid model [23] in which carbon is ablated from the graphite anode in the form of molecules that then evaporate into carbon atoms in the hot arc core. These atoms leave the arc core and travel to the surrounding hot gas region where they associate into small molecules such as C_2 and C_3, which are the basic building blocks for volume growth of nanoparticles in the cooler region outside the region where these species are found. A graphical depiction of this model is shown in figure 4 of [23]. The *in situ* measurements described here support this model.

ORCID iDs

B C Stratton ⓘ https://orcid.org/0000-0001-8830-3003
M N Shneider ⓘ https://orcid.org/0000-0002-2925-7008

References

[1] Kingston C T and Simard B 2003 Fabrication of carbon nanotubes *Anal. Lett.* **36** 3119
[2] Puretzky A A, Geohegan D B, Fan X and Pennycook S J 2000 Dynamics of single-wall carbon nanotube synthesis by laser ablation *Appl. Phys.* A **70** 153
[3] Shashurin A and Keider M 2015 Synthesis of 2D materials in arc plasmas *J. Phys. D: Appl. Phys.* **48** 314007
[4] Arora N and Sharma N N 2014 Arc discharge synthesis of carbon nanotubes: comprehensive review *Diam. Relat. Mater.* **50** 135
[5] Journet C, Maser W K, Bernier P, Loiseau A, de la Chappelle M L, Lefrant S, Deniard P, Lee R and Fischer J E 1997 Large-scale production of single-walled carbon nanotubes by the electric arc technique *Nature* **388** 756
[6] Iijima S and Ichihashi T 1993 Single-shell carbon nanotubes of 1 nm diameter *Nature* **363** 603
[7] Bethune D S, Klang C H, de Vries M S, Gorman G, Savoy R, Vazquez J and Byers R 1993 Cobalt-catalyzed growth of carbon nanotubes with single-atomic-layer walls *Nature* **363** 605
[8] Keidar M, Shashurin A, Volotskova O, Raitses Y and Bellis I I 2010 Mechanism of carbon nanostructure synthesis in arc plasma *Phys. Plasmas* **17** 057101
[9] Shashurin A, Li J, Zhuang T, Keidar M and Bellis I I 2011 Application of electrostatic Langmuir probe to atmospheric arc plasma producing nanostructures *Phys. Plasmas* **18** 073505
[10] Li J, Kundrapu M, Shashurin A and Keider M 2012 Emission spectra analysis of arc plasma for synthesis of carbon

nanostructures in various magnetic conditions *J. Appl. Phys.* **112** 024329

[11] Vekselman V, Feurer M, Huang T, Stratton B and Raitses Y 2017 Complex structure of the carbon arc discharge for synthesis of nanotubes *Plasma Sources Sci. Technol.* **26** 065019

[12] Yatom S, Selinsky R, Koel B and Raitses Y 2017 'Synthesis-on' and 'synthesis-off' modes of carbon arc operation during synthesis of carbon nanotubes *Carbon* **125** 336

[13] Gershman S and Raitses Y 2016 Unstable behavior of anodic arc discharge for synthesis of nanomaterials *J. Phys. D: Appl. Phys.* **49** 345201

[14] Vekselman V, Khrabry A, Kagonovich I, Stratton B, Selinsky R and Raitses Y 2018 Quantitative imaging of carbon dimer precursor for nanomaterial synthesis in the carbon arc *Plasma Sources Sci. Technol.* **27** 025008

[15] Mitrani J and Shneider M 2015 Time-resolved laser-induced incandescence multiwalled carbon nanotubes in air *Appl. Phys. Lett.* **106** 054101

[16] Yatom S, Bak J, Khrabry A and Raitses Y 2017 Detection of nanoparticles in carbon arc discharge with laser-induced incandescence *Carbon* **117** 154

[17] Gerakis A, Shneider M and Stratton B 2016 Remote-sensing gas measurements with coherent Rayleigh–Brillouin scattering *Appl. Phys. Lett.* **109** 031112

[18] Gerakis A, Yeh Y-W, Shneider M, Mitrani J, Stratton B and Raitses Y 2018 Four-wave mixing approach to *in situ* detection of nanoparticles *Phys. Rev. Appl.* **9** 014031

[19] Fang X, Shashurin A, Teel G and Keidar M 2016 Determining the synthesis region of the single wall carbon nanotubes in arc plasma volume *Carbon* **107** 273

[20] Fetterman A J, Raitses Y and Keidar M 2008 Enhanced ablation of small anodes in a carbon nanotube arc plasma *Carbon* **46** 1322

[21] Yeh Y-W, Raitses Y and Yao N 2016 Structural variations of the cathode deposit in the carbon arc *Carbon* **105** 490

[22] Ng J and Raitses Y 2014 Role of the cathode deposit in the carbon arc for the synthesis of nanomaterials *Carbon* **77** 80

[23] Yatom S, Kahrabry A, Mitrani J, Khodak A, Kaganovich I, Vekselman V, Stratton B and Raitses Y 2018 Synthesis of nanoparticles in carbon arc: measurements and modeling *Mater. Res. Soc. Commun.* **8** 1–8

[24] Griem H 1964 *Plasma Spectroscopy* (New York: MacGraw-Hill)

[25] Hutchinson I H 2005 *Principles of Plasma Diagnostics* (Cambridge: Cambridge University Press)

[26] Cau M, Dorval N, Attal-Trétout B, Cochon J L, Foutel-Richard A, Loiseau A, Kruger V, Tsurikov M and Scott C D 2010 Formation of carbon nanotubes: *in situ* optical analysis using laser-induced incandescence and laser-induced fluorescence *Phys. Rev.* B **81** 165416

[27] Cau M, Dorval N, Cao B, Attal-Trétout B, Cochon J L, Loiseau A, Farhat S and Scott C D 2006 Spatial evolutions of Co and Ni atoms during single-walled carbon nanotubes formation: measurements and modeling *J. Nanosci. Nanotechnol.* **6** 1298–308

[28] Dorval N *et al* 2004 *In situ* optical analysis of the gas phase during the formation of carbon nanotubes *J. Nanosci. Nanotechnol.* **4** 450–62

[29] Michelsen H A, Schulz C, Smallwood G J and Will S 2015 Laser-induced incandescence: particulate diagnostics from combustion, atmospheric, and industrial applications *Prog. Energy Combust. Sci.* **51** 2

[30] Snelling D R, Smallwood G J, Liu F, Gulder O L and Bachalo W D 2005 A calibration-independent laser-induced incandescence technique for soot measurement by detecting absolute light intensity *Appl. Opt.* **44** 6773–85

[31] Grinstead J and Barker P F 2000 Coherent Rayleigh scattering *Phys. Rev. Lett.* **85** 1222

[32] Pan X, Shneider M N and Miles R B 2002 Coherent Rayleigh–Brillouin scattering *Phys. Rev. Lett.* **89** 183001

[33] Pan X, Shneider M N and Miles R B 2004 Coherent Rayleigh–Brillouin scattering in molecular gases *Phys. Rev.* A **69** 033814

[34] Gerakis A, Shneider M N and Barker P F 2013 Single-shot coherent Rayleigh–Brillouin scattering using a chirped optical lattice *Opt. Lett.* **38** 4449

[35] Shneider M N and Gimelshein S F 2013 Application of coherent Rayleigh–Brillouin scattering for *in situ* nanoparticle and large molecule detection *Appl. Phys. Lett.* **102** 173109

[36] Santra B, Shneider M and Car R 2017 *In situ* characterization of nanoparticles using Rayleigh scattering *Sci. Rep.* **7** 40230